Available online at www.sciencedirect.com
SCIENCE DIRECT
Journal of Solid State Chemistry 179 (2006) 2663–2673
JOURNAL OF SOLID STATE CHEMISTRY
www.elsevier.com/locate/jssc

Generation of WO_3–ZrO_2 catalysts from solid solutions of tungsten in zirconia

María A. Cortés-Jácome[a], Carlos Angeles-Chavez[a], Xim Bokhimi[b,1], J.A. Toledo-Antonio[a,*]

[a]*Instituto Mexicano del Petróleo. Prog. Ingeniería Molecular, Eje Central L. Cárdenas # 152, 07730 México D.F., México*
[b]*Institute of Physics, The National University of Mexico (UNAM), A. P. 20-364, 01000 México D.F., México*

Received 19 October 2005; received in revised form 13 February 2006; accepted 16 March 2006
Available online 22 May 2006

Abstract

WO_3–ZrO_2 samples were obtained by precipitating zirconium oxynitrate in presence of $WO_4^{=}$ species in solution from ammonium metatungstate at pH = 10.0. Samples were characterized by atomic absorption spectroscopy, thermal analysis, X-ray diffraction, Raman spectroscopy, X-ray photoelectron spectroscopy, high-resolution transmission electron microscopy and energy filtered-TEM. The ammonia retained in the dried sample produced a reductive atmosphere to generate W^{5+} ions coexisting with W^{6+} ions to produce a solid solution of tungsten in the zirconia lattice to stabilize the zirconia tetragonal phase when the sample was annealed at 560 °C. When the sample was annealed at 800 °C, the W atoms near crystallite surface were oxidized to W^{6+}, producing patches of WO_3 on the zirconia crystallite. The HR-TEM analysis confirmed the existence of the solid solution when the sample was annealed at 560 °C, and two types of crystalline regions were identified: One with nearly spherical morphology, an average diameter of 8 nm and the atomic distribution of tetragonal zirconia. The second one had a non-spherical morphology with well-faceted faces and dimensions larger than 30 nm, and the atom distribution of tetragonal zirconia. When samples were annealed at 800 °C two different zirconia crystallites were formed: Those where only part of the dissolved tungsten atoms segregated to crystallite surface producing patches of nanocrystalline WO_3 on the crystallite surface of tetragonal zirconia stabilized with tungsten. The second type corresponded to monoclinic zirconia crystallites with patches of nanocrystalline WO_3 on their surface. The tungsten segregation gave rise to the WO_3–ZrO_2 catalysts.

Keywords: Tungsten zirconia catalysts; Solid solutions; Tetragonal zirconia; XPS; Raman spectroscopy; HR-TEM; EFTEM

1. Introduction

Solid catalysts with strong acidity play an important role in hydrocarbon conversion reactions; for example, in isomerization and alkylation processes [1–4], which involve reactions of great interest in the production of the additives that enhance gasoline octane. Halogen-promoted metal oxides (e.g., chlorinated alumina), liquid acids and strong liquid acids supported onto a porous matrix are the catalysts commercially available for the above applications. These catalysts, however, are unstable, deactivate quickly, and produce corrosive gases with the consequent damage of installations and environment [5–7].

Zirconia modified with sulfate [8], phosphate [9], heteropolyacids HPA [10], tungsten [11], and molybdenum [12] has emerged as an alternative catalysts to substitute chlorinated alumina and liquid acids catalysts. These zirconia based catalysts can be regenerated easily and contain a metal as promoter that generates strong solid acid catalysts able to isomerize n-butane near room temperature [13–15]. From them, tungsten oxide dispersed on zirconia seems to be the most stable and is characterized by having a strong acid sites density [13].

The activation of the catalytic sites depends on synthesis method, where the annealing temperature plays a special role. When coprecipitation [11] and sol–gel [16] methods are used for the synthesis, the samples require higher annealing temperatures for activation than those prepared by impregnation in hydrous zirconia [17]. When these catalysts are prepared by impregnation, all tungsten is on

*Corresponding author. Fax: +52 91756380.
E-mail address: jtoledo@imp.mx (J.A. Toledo-Antonio).
[1]Advisor at the Instituto Mexicano del Petróleo.

0022-4596/$ - see front matter © 2006 Published by Elsevier Inc.
doi:10.1016/j.jssc.2006.03.050

crystallite surface, whereas in coprecipitated and sol–gel synthesis methods it is assumed that W atoms incorporate into ZrO_2 lattice, stabilizing the tetragonal structure [11,16]. Both synthesis methods require high temperatures to have tungsten oxide on zirconia crystallites surface. Because tungstate species entrapped in the bulk of the zirconia must be expelled onto the surface [16–18], little attention has been paid to explain how the W atoms remain in the ZrO_2 lattice stabilizing the tetragonal structure. Zirconia surface stabilization mechanism by oxoanions such as, tungstate, molybdate, or sulfate, is to date, the most accepted hypothesis, establishing coverage of WO_x species of a ZrO_2 core. These WO_x species have been postulated on basis of the local environment around the W atoms, where the oxygen coordination numbers assume values of 4 for a tetrahedral and 6 for an octahedral coordination. The possibility of the W atoms reduction to form solid solution with ZrO_2 at low temperature has not been yet considered, this subject will be addressed in this work.

Recently we reported that tungsten and zirconia oxide form solid solutions below 800 °C, stabilizing zirconia in two tetragonal crystalline phases [20] that differ mainly in the oxygen position along the *c*-axis. In the phase with higher symmetry this position is at 0.50(2), producing flat crystallite surfaces perpendicular to the *c*-axis, while in the phase with the lower symmetry it is at 0.447(2), giving rise to rough crystallite surfaces parallel to (100) planes. When the sample is annealed at 800 °C its acid site density is two times higher than when it is prepared by impregnation [11]; it seems that the segregation of tungsten atoms from the crystallite bulk to its surface determines the WO_x species on it.

In the literature it is assumed that the high acid site density obtained in the zirconia system after calcining samples above 850 °C is due to the coverage of crystallites surface with a monolayer of WO_3 [13,16,21]. When tungsten content is higher than the ideal amount to produce only one monolayer, it gives rise to three-dimensional WO_x species [21] that produce a higher isomerization activity than the ones formed in the WO_x/Al_2O_3 system [22]. The preparation techniques used are devoted specially for designing microstructure of WO_x species on the surface of ZrO_2, which is thought to be useful for catalysis. The possibility of formation of solid solution $(WZr)O_2$ at certain stage of the preparative treatment procedure has been scarcely considered in the literature.

In the present work, the thermal evolution of crystalline phases generated in the WO_3–ZrO_2 system was analyzed by using, thermal analysis (TGA-DTA), X-ray diffraction (XRD), Raman spectroscopy, X-ray photoelectronic spectroscopy (XPS), Energy filtered transmission electron microscopy (EFTEM), high resolution transmission electron microscopy (HR-TEM) and X-ray energy dispersive spectroscopy (EDS), which complement our previous study on the system made with X-ray diffraction and refinement of the crystalline structure [20]. The present work gives additional experimental evidence about the formation of the solid solution of tungsten atoms into zirconia lattice to produce two zirconia tetragonal phases, and their further transformation into monoclinic zirconia and orthorhombic WO_3 phases when the sample was annealed at 800 °C.

2. Experimental

2.1. Synthesis

Mixed zirconium tungsten hydroxide was prepared from an aqueous solution of zirconium oxynitrate, $ZrO(NO_3)_2 \cdot 6H_2O$ (Aldrich 99%), and ammonium metatungstate hydrate, $(NH_4)_6W_{12}O_{39} \cdot xH_2O$ (Aldrich 99%). Precipitation was carried out at pH 10 with an aqueous solution of ammonium hydroxide 14 vol% of NH_4OH (J.T. Baker, 28 vol%). The ammonium metatungstate solution was placed in a 4 L container, and the pH was adjusted to 10.0 by adding some drops of ammonium hydroxide solution, in order to have $WO_4^{=}$ species in solution [23]. Thereafter, the zirconium oxynitrate solution was added by dropping together with the remaining ammonium hydroxide solution maintaining the pH constant at 10.0. Herein, a white slurry was obtained by precipitating ZrO_2 in presence of $WO_4^{=}$ species, which must be entrapped in the $Zr(OH)_4$ precipitate.

The obtained white slurry was aged for 24 h at room temperature; then, it was filtered and dried at 110 °C in a vacuum for 18 h (fresh sample). Thereafter, the fresh sample was annealed at 560 °C or 800 °C for 4 h in flowing air.

2.2. Characterization

Elemental analysis was determined on the sample annealed at 800 °C by atomic absorption spectroscopy (AAS) with a Perkin–Elmer 5000 spectrophotometer.

Differential thermal analysis (DTA) was developed on Perkin–Elmer ATD 1700 apparatus from room temperature to 1000 °C. Weight loss curves were determined by Thermogravimetry (TGA) with a Perkin–Elmer TG-7 in the as synthesized sample. The heating rate was 5 °C/min, from room temperature to 1000 °C, flowing air at 20 cm^3/min.

The X-ray diffraction patterns of the samples packed in a glass holder were recorded at room temperature with CuKα radiation in a Bruker Advance D-8 diffractometer having θ–θ configuration and a graphite secondary-beam monochromator. Diffraction intensity was measured in the 2θ range between 15° and 110°, with a 2θ step of 0.02° for 8 s per point.

The Raman spectra were recorded at room temperature using an Yvon Jobin Horiba (T64000) spectrometer, equipped with a confocal microscope (Olympus, BX41) with a laser 514.5 nm emission line at a power of 15 mW. The spectrometer is equipped with a CCD detector.

X-ray photoelectron spectroscopy (XPS) spectra were recorded on a THERMO-VG scalab 250 spectrometer equipped with AlKα X-ray source (1486.6 eV) and a hemispherical analyzer. The base pressure during the analysis was 10^{-9} Torr. The XPS analyses were performed in a static system, on the samples after their calcining. The experimental peaks were decomposed into components using mixed Gaussian-Lorentzian functions, non-linear squares fitting algorithm and Shirley-type background subtraction by using XPS peak fit software. The binding energies (BE) were referenced to the adventitious carbon C (1 s) peak at 284.6 eV. Changes in the $W_{4f}+Zr_{4p}$ signal shape on the samples calcined at different temperatures were analyzed by a curve fitting-procedure with doublets endowed with fixed spectroscopic parameters, but using variable position, full width at half maximum (FWHM) and intensities. The spectroscopic parameters used were taken from literatrure [17]: $W(4f_{7/2})$–$W(4f_{5/2})$, spin orbit separation 2.1 eV and intensity ratio $R = 0.75$; $Zr(4p_{3/2})$–$Zr(4p_{1/2})$, spin–orbit separation, 1.78 eV and intensity ratio $R = 0.5$.

High-resolution transmission electron microscopy and the EDS analysis of the samples were performed in a JEOL 2010F transmission electron microscope operating at 200 kV, and equipped with a Schottky-type field emission gun and an ultrahigh resolution pole piece ($C_s = 0.5$ mm; point to point resolution, 0.190 nm). The energy filtered transmission electron microscopy (EFTEM) was performed in a Tecnai G^2 F30 S-Twin transmission electron microscope operating at 300 kV equipped with a GATAN GIF/PEELS system for EFTEM that was controlled by Gatan Digital Micrograph. The slit width of the energy filter is fixed for major element-specific edges in the electron energy loss spectrum (EELS), and the intensity at each pixel is integrated using the Gatan Imaging Filter (GIF). The final elemental map is produced after the subtraction of background as determined by two pre-edge images. As EFTEM is based on EELS, the intensity of elemental maps varies depending on the element, edge selection, specimen thickness, and electronic structure of the material [24].

For the electron microscope analysis, the samples were pulverized, suspended in isopropanol at room temperature, and dispersed with ultrasonic agitation; then, an aliquot of the solution was dropped on a 3 mm diameter lacey carbon copper grid. Fourier transform (FT) patterns of the HR-TEM micrographs were performed to obtain the interplanar distances in order to identify the tetragonal and monoclinic phases of the ZrO_2 by comparing these distances with those reported for these phases in the JCPDS cards no. 42-1164 and 37-1484, respectively.

3. Results and discussion

Elemental analysis determined by AAS showed that the calcined sample contain 11.6 wt% of tungsten, which correspond to a 14.6 wt% of WO_3. Considering that the theoretical amount of W atoms loaded in the synthesis was 15.0 wt%, and that at pH = 10 the tungsten remain mainly as $WO_4^{=}$ species in solution [23], only 77% of the total $WO_4^{=}$ species interact with the zirconium hydroxide and remain bonded into the zirconium dried gel, the rest was eliminated in the liquor.

Differential thermal analysis showed two exothermic peaks centered at 279 and 560 °C, Fig. 1. The first one occurred at the same temperature that the main weight loss attributed to the dehydroxilation, nitrate and ammonia removing was observed. This exothermic peak was attributed to the oxidation of the removed ammonia species, which gives rise to the formation of W^{5+} ions that coexist with W^{6+} ions. The second exothermic peak occurs once the dehydroxilation have finished (Fig. 1): It is attributed to crystallization of the zirconia tetragonal phase. In fact, the samples prepared by impregnation of ammonium metatungstate over omorphous $Zr(OH)_4$ only showed one peak attributed to the crystallization of the tetragonal phase at lower temperatures. Since the zirconia crystallization peak occurred at 560 °C, the samples were annealed at this temperature; they were further annealed at 800 °C to analyze the zirconia phase transformation and its stability.

The X-ray diffraction patterns of the as-synthesized samples showed that they had only the amorphous phase that corresponded to the hydroxylated zirconia (Fig. 2). A well-crystallized tetragonal phase was obtained when the sample was annealed at 560 °C, while the tetragonal and monoclinic zirconia phases were obtained when the precipitate was annealed at 800 °C. At this temperature also a small amount of orthorhombic WO_3 was generated suggesting that part of the tungsten atoms remain dissolved in the zirconia bulk stabilizing it in the tetragonal phase. When W atoms were segregated as orthorhombic WO_3 phase, the corresponding tetragonal zirconia phase transforms into the monoclinic one. Direct evidence of these asseverations will be given through the analysis of the EFTEM and HRTEM micrographs.

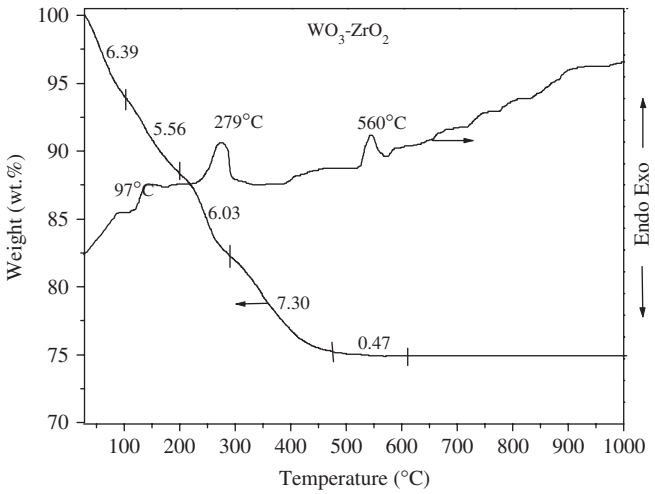

Fig. 1. DTA and TGA curves of WO_3–ZrO_2 dried sample.

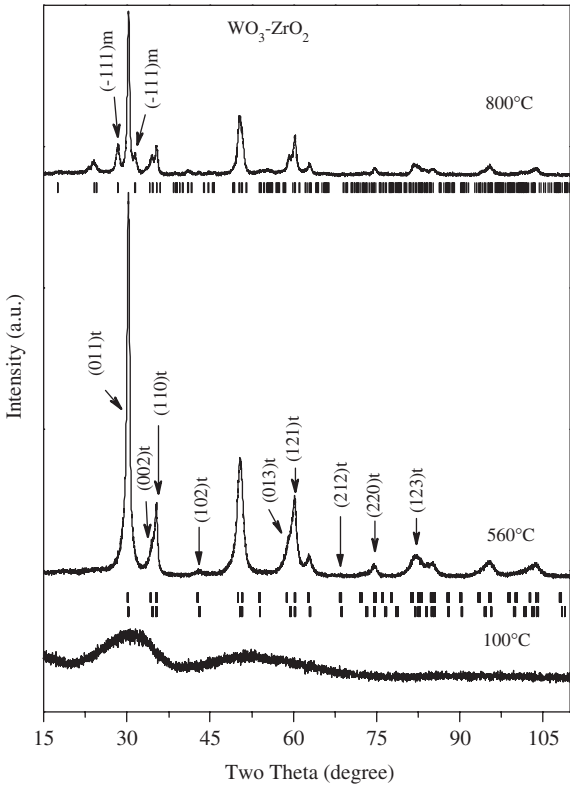

Fig. 2. X-ray diffraction patterns of WO_3–ZrO_2 samples annealed at temperatures between 100 and 800 °C. Upper tick marks below the diffraction pattern of the sample annealed at 800 °C correspond to monoclinic zirconia, their corresponding Miller indices are marked with "m". Middle tick marks below the diffraction pattern of the sample annealed at 560 °C correspond to tetragonal zirconia; their corresponding Miller indices are marked with a "t". For clarity, the diffraction pattern of the amorphous phase was magnified.

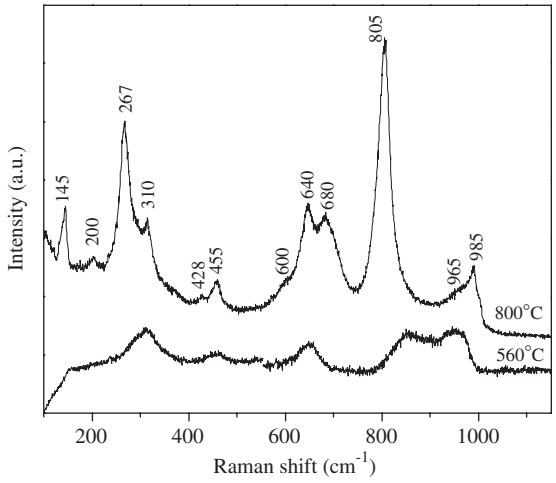

Fig. 3. Raman spectra of the WO_3–ZrO_2 samples annealed at 560 and 800 °C.

The Raman spectra confirmed the presence of the zirconia phases observed by XRD. In the samples annealed at 560 °C, the tetragonal ZrO_2 phase was identified by the presence of the absoption bands at 310, 455, and 640 cm^{-1} (Fig. 3). In the sample annealed at 800 °C, additional to the bands of tetragonal phase, other low intensity bands corresponding to monoclinic ZrO_2 phase [25] were observed at 200, 428 and 600 cm^{-1}.

Two types of tungsten atom environments were detected by Raman spectroscopy (Fig. 3). In the sample annealed at 560 °C, two broad bands at 830–890 and 930–985 cm^{-1} appeared, which are likely to arise from bridging W–O and terminal W═O stretching modes [21,26]. These bands have been assigned to polyoxo anionic species well dispersed WO_x on the tetragonal zirconia and variation in their position gave rise to broadened signals revealing various environments of the WO_x species [26]. On the other hand, these bands have also been attributed to tungstate species entrapped in the bulk of aerogels [16]. The vibrating bands corresponding to W–O–W deformation mode and W–O bending mode around 275 and 680–720 cm^{-1} respectively, were not observed in the sample calcined at 560 °C, suggesting the presence of isolated tungstate species diluted into the tetragonal ZrO_2. In the sample annealed at 800 °C, the broad band around 830–890 cm^{-1} shifted to lower position at 805 cm^{-1}, increasing its intensity and resolution, which is characteristic of the W–O stretching mode in WO_3 nanoparticles [21]. An additional band at 680 cm^{-1} appeared which has been assigned to the W–O bending mode. The band characteristic to the W–O–W deformation mode occurred at 267 cm^{-1}. These bands did not appear in the samples annealed at 560 °C and are attributed to the growing of three-dimensional nanocluster of crystalline WO_3 in agreement with our XRD results.

The XPS spectrum of the calcined samples showed significant differences in the shape of the W(4*f*) + Zr(4*p*) region (Fig. 4). The W(4*f*) doublet of the sample annealed at 560 °C became broader and a tail appeared at low BE side, overlapping with the Zr(4*p*) component (Fig. 4a). Whereas, the W(4*f*) doublet of the sample calcined at 800 °C, Fig. 4b, was more separated and less overlapped with the Zr(4*p*) component. The spectra of both samples were fitted with two doublets to account the whole W (4*f*) region, besides a doublet corresponding to the Zr(4*p*) component. The BE values of the doublets were assigned to different oxidation state of W atoms according to literature data [27]. The BE values reported for W^{6+} atoms is 35.6 ± 0.2 eV, while the BE values reported for W^{5+} is 34.8 ± 0.3 eV. In the sample annealed at 560 °C, Fig. 4a, the larger doublet occurred at 34.8 and 36.9 eV for the W(4*f*) spin-orbit components, which is attributed to W^{5+} atoms; the second one at 35.8 and 37.9 eV corresponds to W^{6+} atoms, with a W^{6+}/W^{5+} ratio of 42/58 (0.72) (Table 1). On the other hand, in the sample calcined at 800 °C the larger doublet was that assigned to W^{6+} occurring at 35.3 and 37.4 eV, and the lower one at 34.5 and 36.6 eV is that assigned to W^{5+}, with a W^{6+}/W^{5+} ratio of 69/31 (2.23) (Table 1). Later parameters derived from the XPS curve fitting indicated that tungsten oxidation state depends on the calcination temperature, i.e. the higher amount of reduced W^{5+} atoms the lower calcination temperature.

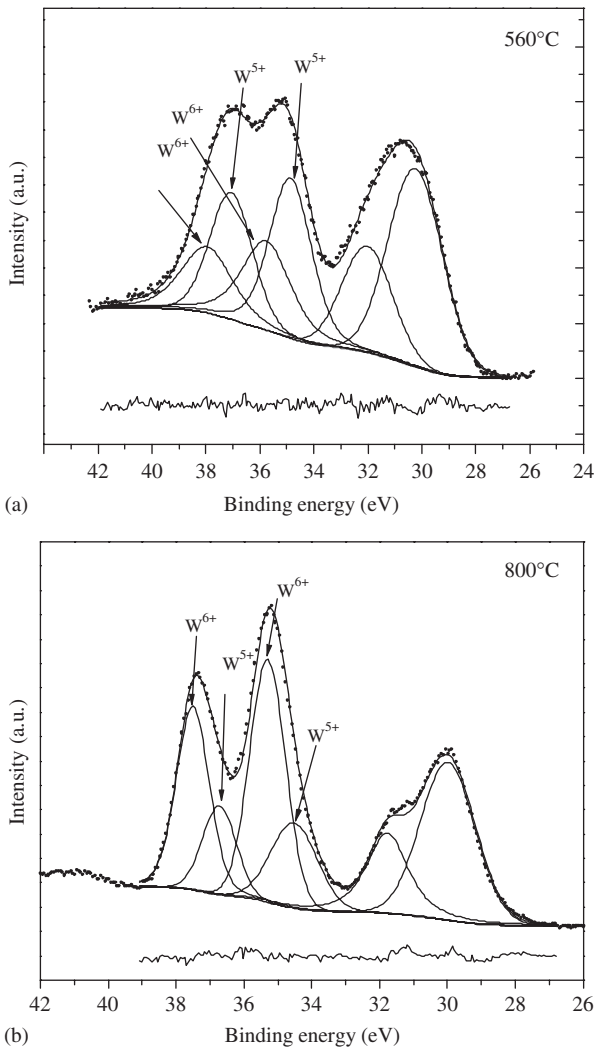

Fig. 4. XPS of W(4*f*) + Zr(4*p*) region of WO_3–ZrO_2 samples after their annealing at 560 °C (a) and 800 °C (b).

Table 1
XPS Parameters of the W(4*f*) region in WO_3–ZrO_2 samples annealed at 560 and 800 °C

T (°C)	BE (eV)	Assignment	W (%)	W^{6+}/W^{5+}	W (at%)	Zr (at%)	W/Zr
560	35.79	W^{6+}	41.77	0.72	4.53	23.21	0.195
	34.85	W^{5+}	58.22				
800	35.29	W^{6+}	68.65	2.23	6.38	25.15	0.254
	34.52	W^{5+}	31.35				

The W/Zr surface atomic ratio, also presented in Table 1, increased from 0.19 to 0.25 for the sample annealed at 560 and 800 °C, respectively, which means an increase in the concentration of W atoms on the surface of ZrO_2. As the amount of the W atoms is constant in the sample, the increase of the W/Zr ratio with the annealing temperature must correspond to the migration of W atoms from the bulk to the ZrO_2 surface. The fact that the W oxidation state changes from W^{5+} to W^{6+} with the annealing temperature, indicate that W atoms diluted in the bulk of ZrO_2 [16,18,19] remain in a reduced oxidation state lower than W^{6+}. Given the quantitative reduction of tungsten atoms to W^{5+}, it is possible to propose the formation of a kind of solid solution with the formula $Zr_{1-x}W_xO_{2+x/2}$, at least in the first layers of the crystal structure. The W atoms remained reduced precisely because they are occluded in the ZrO_2 bulk, the leave of the W atoms to the surface involve their oxidation to W^{6+}.

Then, the tetragonal structure is stabilized by these reduced species (W^{5+}) diluted in the bulk of the ZrO_2, changing the symmetry and originating a second tetragonal phase, such as was observed in our XRD Rietveld Refinement data [20]. In fact the concentration of these W^{5+} reduced atoms (58%) and W^{6+} atoms (42%) determined by XPS, Table 1, correspond to the concentration of the two tetragonal phases used to model the XRD patterns, which was 59% and 41%. Therefore, the presence of these two mismatched tetragonal phases can be explained by the concentration gradients of tungsten atoms from inside to outside the tetragonal ZrO_2 particles. Direct evidence of W atoms evolution from ZrO_2 bulk to surface will be done by EFTEM images.

From our Raman and XPS results, it can be concluded that the two broad bands at 830–890 and 930–985 cm^{-1} (Fig. 4), must be assigned to the bridging W–O and terminal W=O stretching modes, the variation in positions and broadened signals must be attributed to the different oxidation states of the W atoms.

The tungsten distribution in the ZrO_2 crystallites was studied by EFTEM. For W atoms the energy filter images were obtained with the O1-edge, and for the Zr atoms with the M45-edge. The TEM image of the sample calcined at 560 °C showed two different particles: the small spherical particles, marked by black arrows, and big particles shown in Fig. 5a. The EFTEM images corresponding to W and Zr atoms on this crystal region are presented in Figs. 5b and c, respectively. The chemical dispersion of both elements was obtained by mixing the W and Zr maps EFTEM, Fig. 5d. It is interesting to note that there is not enrichment of W atoms at the borders of the crystallites; in contrast, in the crystallite presented in Fig. 5a, Zr atoms were at the crystallite border (Fig. 5d): The W atoms are mixed with the Zr atoms inside the crystallite. This result confirm the hypothesis of a solid solution mechanism claimed in our previous work [20].

When the sample was calcined at 800 °C, the TEM image showed more homogeneous crystallites with dark contrast patches decorating the surface, Fig. 6a. The EFTEM images corresponding to W and Zr atoms in these crystallites are presented in Figs. 6b and c, respectively. The chemical dispersion of both elements was obtained by mixing the W and Zr maps, Fig. 6d. In contrast to the observation on the sample calcined at 560 °C, in the sample calcined at 800 °C, a high W atoms concentration was observed at the border of these crystallites forming a

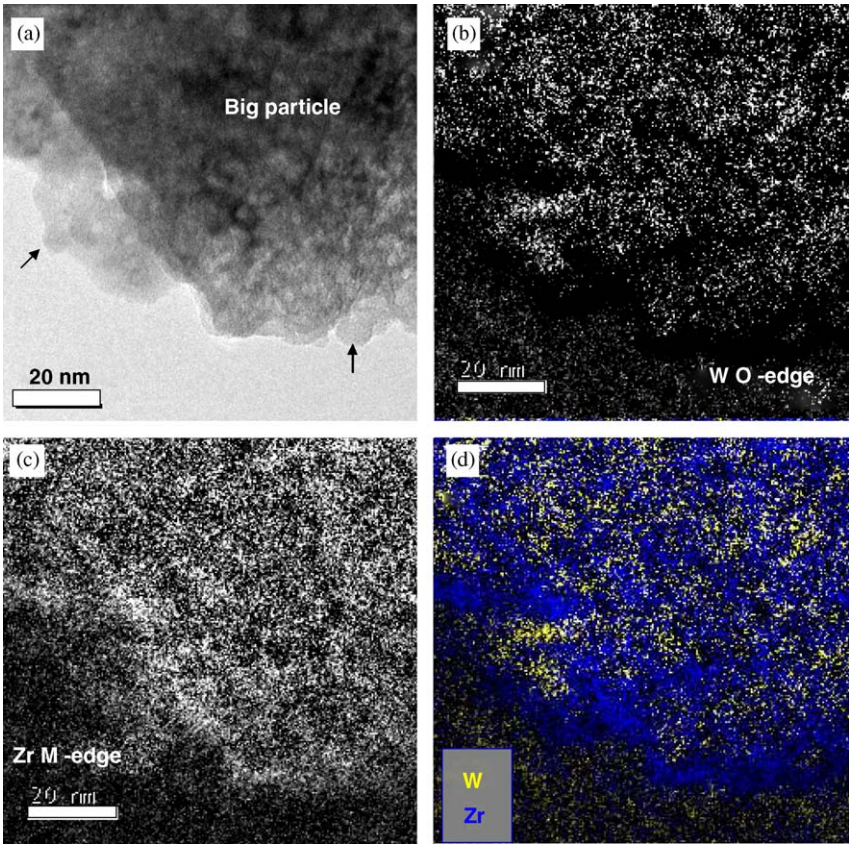

Fig. 5. EFTEM micrographs of the sample annealed at 560 °C: (a) Bright field image, (b) filtered image of W obtained with O1-edge, (c) filtered image of Zr obtained with M45-edge, and (d) image obtained by mixing the W and Zr filtered images.

coverage of W atoms on the ZrO_2 core, Fig. 6d. The thickness of the W atoms layer on the surface is approximately 2.0 nm. Then, the W atoms remained initially inside the crystallite after annealing at 560 °C in a reduced oxidation state (W^{5+}), whereas, the sample annealed at 800 °C the W atoms migrate from the bulk to the surface, forming a layer of W atoms on a ZrO_2 core, with the consequent oxidation to W^{6+}.

The HRTEM micrographs of the samples calcined at 560 °C show that they contained two different types of well defined crystalline regions: One where the crystallites were nearly spherical with an average diameter of 8 nm (Fig. 7), and another characterized by non-spherical crystallites that have well-faceted faces and dimensions larger than 30 nm (Fig. 8); both types of crystallites had the symmetry of tetragonal zirconia. This result was according to the one reported for the X-ray diffraction analysis of these samples, where two different tetragonal phases with different crystallite size and almost the same concentration were observed [20]. It is important to remark that the small crystalline regions do not correspond to single particles; they are embedded in larger particles.

The elemental analysis of the crystalline regions using the EDS technique available in the field emission transmission electron microscope show that the crystallites with spherical symmetry has a larger tungsten concentration than the faceted crystallites. In average, the spherical crystallites contained 12.5 mol% WO_3, while the well-faceted crystallites contained 9 mol% WO_3.

Since the EFTEM and high-resolution images show uniform distribution of the dispersing atoms in the crystallines, the tungsten atoms in the crystallines must be dissolved in the zirconia lattice forming a solid solution. This confirms the propositions made from the X-ray study of these samples [20] that tungsten forms a solid solution in the zirconia lattice stabilizing the tetragonal phase of this oxide.

It is well known that the high symmetry phases of zirconia is stabilized when it is doped with specific ions; for example, La [28], Ca [29], Ce [30], or Y [31], the symmetry is higher as the ion concentration increases. Therefore, it is correct to assume that the symmetry of the zirconia lattice behaves similarly when tungsten is the stabilizing element—specific experiments varying tungsten concentration, however, must be done to test it. Assuming that this is true, the spherical crystalline regions described in the above paragraphs should have a higher atomic distribution symmetry than the corresponding one of the faceted crystallites.

A systematic study of nanocrystalline zirconia stabilized with yttrium shows that the crystallite size decreases as the yttrium concentration and the lattice symmetry increases [31]. If this behavior is similar when tungsten atoms are the structure stabilizers, then the smaller crystalline regions

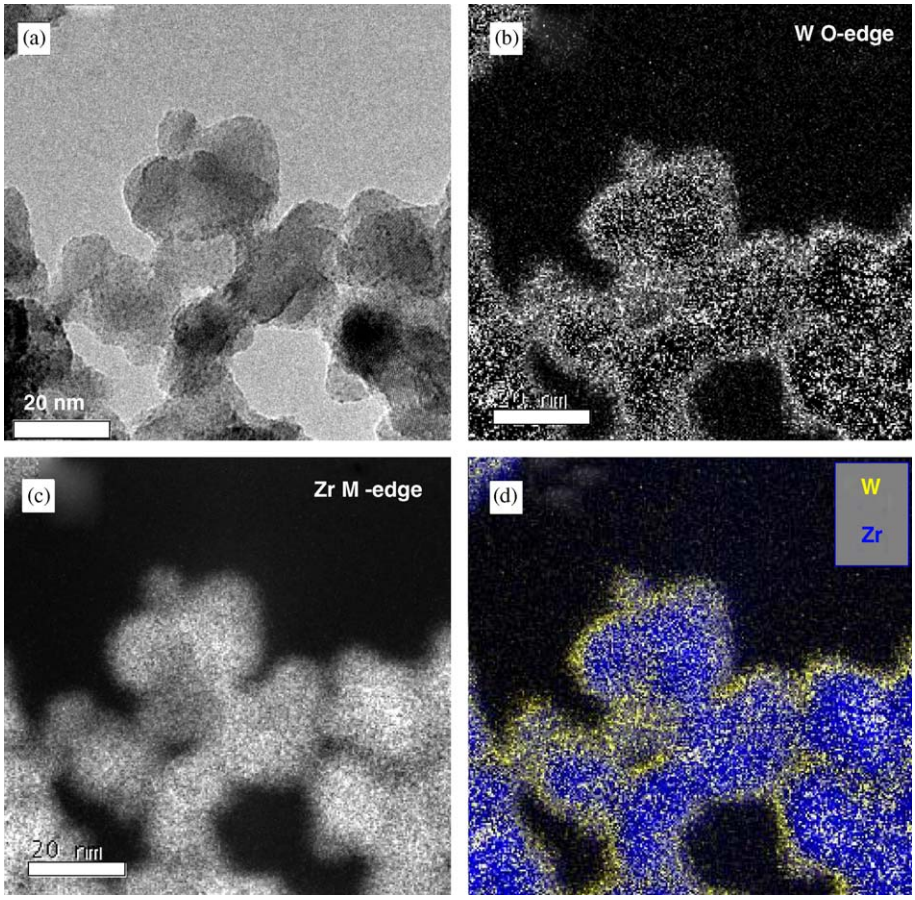

Fig. 6. EFTEM micrographs of the sample annealed at 800 °C: (a) Bright field image, (b) filtered image of W obtained with O1-edge, (c) filtered image of Zr obtained with M45-edge, and (d) IMAGE obtained by mixing the W and Zr filtered images.

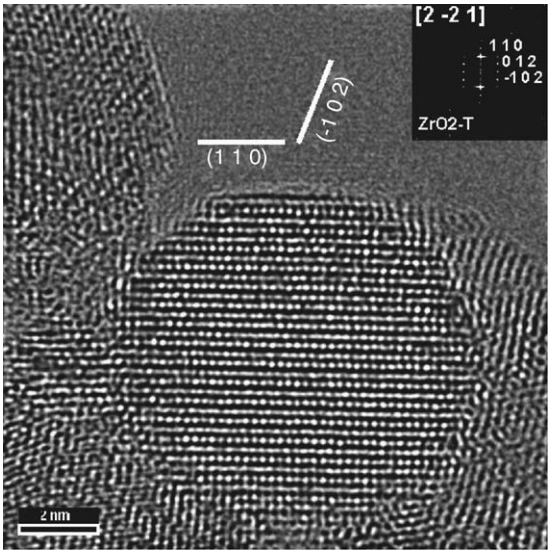

Fig. 7. HR-TEM micrograph of the sample annealed at 560 °C, taken along the [2$\bar{2}$1] zone axis of the tetragonal zirconia lattice. It shows a quasispherical crystallite of the tetragonal zirconia phase. The inset corresponds to the absolute value of the Fourier transform of the image.

(the ones with spherical symmetry), which had the highest tungsten concentration, should have a larger crystalline lattice symmetry than the crystallite with faceted surfaces.

It is interesting to note that the crystalline regions with higher tungsten content had less lattice defects than the crystallites with the lower tungsten concentration, which had inclusive dislocations (Fig. 8). Tungsten substitution for zirconium atoms in the lattice affected locally (many unit cells) crystalline structure, this is an effect mainly due to the difference between tungsten and zirconium valences, than to their difference in atomic sizes [32]. The borders of the crystalline regions were almost defect free, this is more clear in the faceted regions because part of them had the vacuum as background and could be analyzed in detail (Fig. 8); their facets were flat.

This contrasts with the behavior of the crystalline regions when the sample was annealed at 800 °C. Here, many dark patches made of tungsten oxide appeared on the zirconia crystallites surface. After annealing the sample at this temperature three different crystalline phases were observed: Tetragonal zirconia, monoclinic zirconia and orthorhombic WO_3, which is according with the reported X-ray diffraction data for these samples [20].

In the low-magnification micrographs of these samples taken with a small defocussing to highlight the roughness of zirconia crystallites surface, which was exclusive of the samples annealed at this temperature, crystallites seemed to be decorated by small black nanoclusters (Fig. 9), made (according to the EDS analysis) of tungsten and oxygen

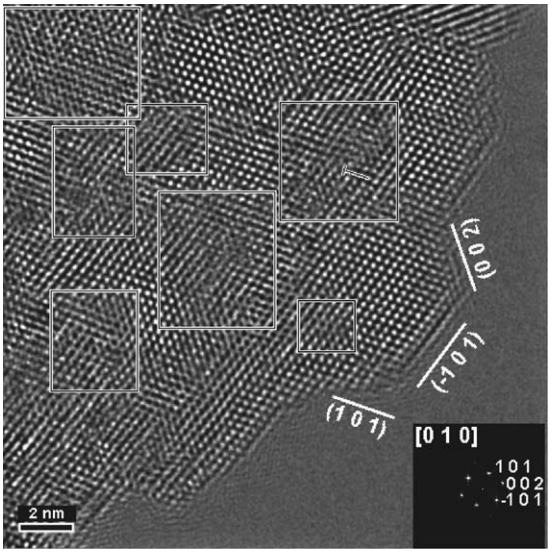

Fig. 8. HR-TEM micrograph of the sample annealed at 560 °C, taken along the [010] zone axis of the tetragonal zirconia lattice. It shows a crystallite, with many lattice defects, of the tetragonal zirconia phase with large crystallite size. The inset corresponds to the absolute value of the Fourier transform of the image.

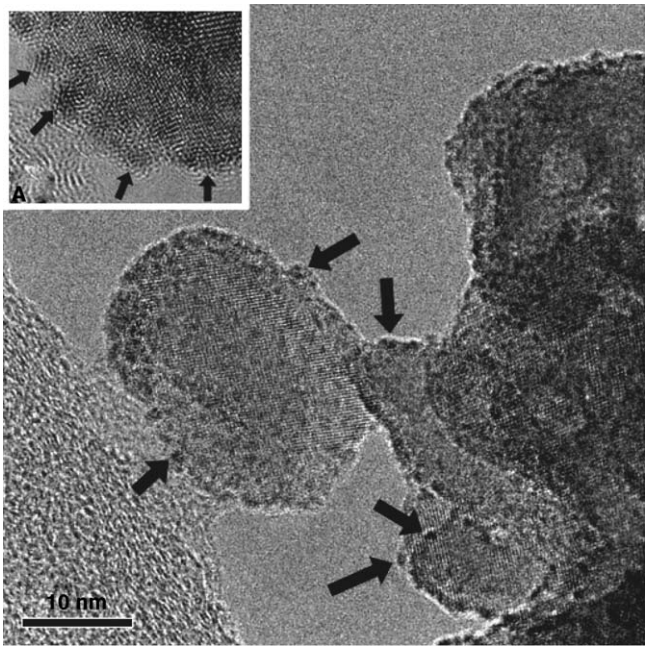

Fig. 9. TEM micrograph of the sample annealed at 800 °C showing zirconia crystallites decorated by dark tungsten oxide nanocluster on its surface, some of them marked with black arrows. The inset is a HR-TEM micrograph that details the tungsten oxide nanoclusters on crystallite surface.

atoms, distributed on zirconia crystallites surface. This result contrasts with the reported claims [33,34], which assume that WO_3 form a monolayer film on zirconia crystallite surface. The inset in Fig. 9 shows details of these nanoclusters; they were produced by the segregation of the tungsten atoms in the tetragonal zirconia phases from the bulk to crystallite surface. This result is according with the X-ray diffraction pattern of the sample annealed at 800 °C, which contains tungsten oxide as one of its phases [20].

According to the XPS results, when the sample was annealed at 560 °C, the tungsten atoms were dissolved in the zirconia matrix as W^{5+} and W^{6+} in a proportion of 58 and 42, respectively. As the annealing temperature of the sample was raised to 800 °C the most external W^{5+} ions oxidized and destabilizing the zirconia lattice, which produced their migration to crystallite surface as W^{6+} ions. Therefore, the sample annealed at this temperature had a higher W^{6+} concentration (Fig. 4b, and Table 1). The migration of the tungsten atoms to the surface produce patches of WO_3 on crystallite surface, and if the rest of tungsten atom in the corresponding crystallite is small, its crystalline structure transforms producing monoclinic zirconia.

Since the valences of tungsten atoms are larger than the valence of zirconia, when they are dissolved in the zirconia lattice, a lot of cation vacancies should be formed to maintain the electrical neutrality of the crystal.

The high-resolution TEM micrograph, taken along [13$\bar{1}$] zone axis, of a tetragonal zirconia crystallite generated after annealing the sample at 800 °C (Fig. 10) clearly shows the presence of the WO_3 patches on crystallite surface. The crystallite borders associated to the (101) and ($\bar{1}$12) planes of the crystallite were not flat as claimed by some authors [35]. They were rough caused by the patches of tungsten nanoclusters with dimensions smaller than 1.5 nm, as indicated by the black arrows in the micrograph. These patches did not cover the full crystallite surface, in contradiction with the published assumptions that tungsten oxide formed a continuous monolayer on this surface [33]. The micrograph also shows that tungsten oxide patches

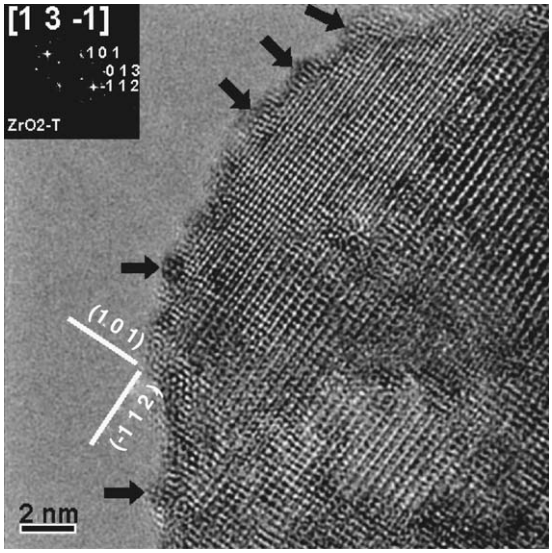

Fig. 10. HR-TEM micrograph of the sample annealed at 800 °C, taken along the [13$\bar{1}$] zone axis of the tetragonal zirconia lattice. Zirconia crystallite surface was decorated with nanoclusters of tungsten oxide indicated with black arrows. The inset corresponds to the absolute value of the Fourier transform of the region of the image corresponding to the crystallite.

grew preferentially on the surface generated by ($\bar{1}12$) planes of the tetragonal zirconia. Since tetragonal zirconia at room temperature, at which the sample was analyzed, only exists when it is stabilized with doping atoms, the above result indicates that only part of the dissolved tungsten atoms in the zirconia lattice, formed when the sample was annealed at 560 °C, segregated to the surface while the rest of them stayed in zirconia lattice stabilizing its tetragonal structure.

The high-resolution TEM micrograph, taken along [3$\bar{1}$5] zone axis, of a monoclinic zirconia crystallite in the sample annealed at 800 °C shows that crystallite surface was not flat (Fig. 11). As in the tetragonal crystallites in this sample, the surface of the monoclinic crystallites was covered with patches of tungsten oxide, whose size depended on the crystallite surface on which they grew; for example they were between 2 and 3 nm when they grew on the surface generated by ($\bar{1}$21) planes; the distance between these patches was also large, which, as it will be evident in the following paragraphs, was intrinsic to the atom distribution on this surface. Since all crystallites in the sample annealed at 560 °C corresponded to tetragonal zirconia, the crystallites with the monoclinic structure of zirconia observed at 800 °C should correspond to those crystallites where almost all tungsten atoms segregated from their bulk to their surface.

In order to analyze the nearly crystalline atom distribution of the tungsten oxide nanoclusters on the monoclinic zirconia crystallite, the FT of the region enclosed in the micrograph was performed (Fig. 12); this revealed the interplanar distances of 0.224, 0.204 and 0.165 nm, which according to the JCPDS card no. 20-1324 and a crystallographic analysis, corresponded to the interplanar distances of the (22$\bar{1}$), (112) and (331) planes of the orthorhombic WO_3 phase, demonstrating that the

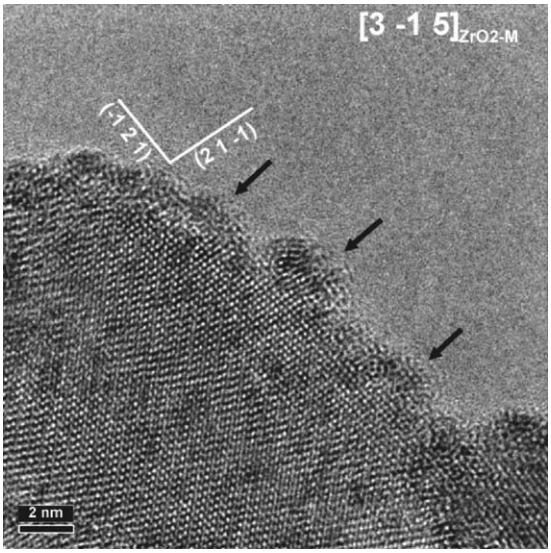

Fig. 11. HR-TEM micrograph of the sample annealed at 800 °C, taken along the [3$\bar{1}$5] zone axis of the monoclinic zirconia lattice. Zirconia crystalline surface was decorated with nanoclusters of tungsten oxide.

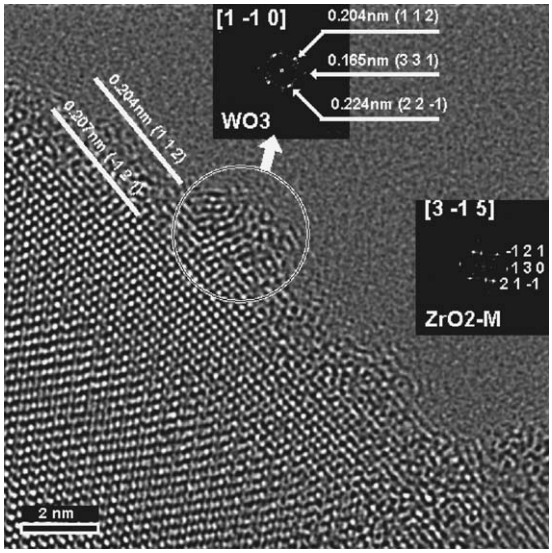

Fig. 12. HR-TEM micrograph of the sample annealed at 800 °C, taken along the [3$\bar{1}$5] zone axis of the monoclinic zirconia lattice. It shows a monoclinic zirconia crystallite with deformed nanocrystallites of WO_3 phase on its surface. The insets correspond to the absolute value of the Fourier transform of two different image regions: One of a WO_3 nanocrystallite, and the other of the monoclinic zirconia crystallite.

nanoclusters on the zirconia crystallites surface were made of orthorhombic WO_3, which is in accordance with the X-ray analysis of the sample [20].

A detailed analysis of the nanocrystallites of WO_3 on monoclinic zirconia crystallites (Fig. 12) shows that the (112) planes of the tungsten oxide phase were parallel to the ($\bar{1}$21) planes of the monoclinic zirconia phase.

The analysis of these ($\bar{1}$21) planes at an atomic level shows that the atomic arrangement cannot give rise to a flat crystallite surface (Fig. 13), which obviously would hinder the possibility of a epitaxially growing of WO_3 on this surface, because this surface is not flat, like the one defined by (111) planes of copper, for example. The above analysis shows that the problem of growing a monolayer of tungsten oxide on zirconia crystallites is not only a question of the difference of atom bond lengths in both phases, which typically occurs in epitaxial growing, but also of the intrinsic roughness of zirconia crystallites surface.

Therefore, the most stable morphology of tungsten oxide growing on zirconia crystallite surface corresponds to islands forming patches on the zirconia crystallite surface; islands diameters were determined by the intrinsic roughness of zirconia surface, which causes large strains on the first layers of the tungsten oxide nanocrystallites. Additional tungsten migration to the surface increased islands dimensions perpendicular to zirconia crystallites surface, forming patches with a pyramid like form.

To explain the nature of the active sites in WO_3–ZrO_2 catalysts, several authors [34,36] claim that tungsten atoms are homogeneously distributed on the surface of the zirconia phases, forming a monolayer of WO_x on the

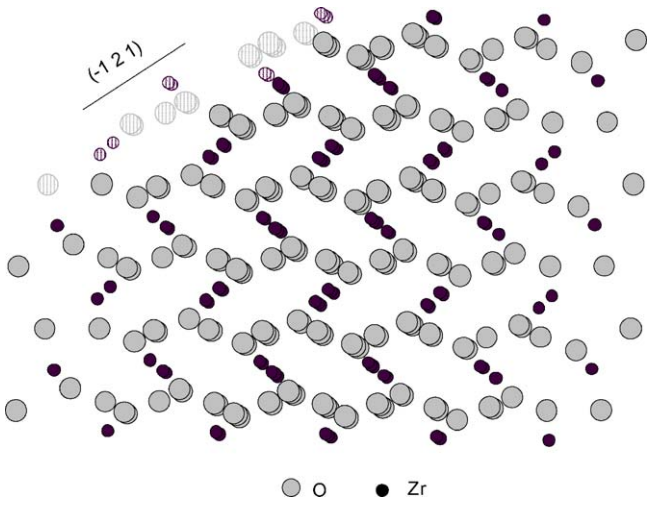

Fig. 13. Projection of the monoclinic zirconia lattice along [3$\bar{1}$5] zone axis. It shows that ($\bar{1}$21) planes cannot give rise to a flat crystallite surface.

ZrO_2 surface. From the results obtained in this work, it is clear that the WO_3 phase is not distributed homogeneously on the ZrO_2 surface, but in the form of patches of WO_3 nanocrystallites, with dimensions between 1.5 and 3 nm, decorating the surface of the ZrO_2 nanocrystallites, and producing a highly defective surface responsible for the high catalytic activity [36–39].

4. Conclusions

WO_3–ZrO_2 catalyst was synthesized by precipitation of zirconium oxynitrate in presence of $WO_4^{=}$ species in solution at pH = 10.0. During precipitation, tungsten species, nitrate and ammonia ions are entrapped into de amorphous hydroxide. During the calcination procedure of the sample the removal of ammonia ions create a reductive atmosphere that give rise to W^{5+} coexiting with non-reduced W^{6+} ions. The reduction created the conditions for the solution of W atoms in the zirconia lattice with many cation vacancies; tungsten atoms stabilize the tetragonal structure of zirconia.

When the sample was annealed in air at 800 °C, the W^{5+} ions near the surface oxidize to W^{6+} making the lattice unstable and producing their migration to the crystallite surface to generate patches of WO_3. This migration causes the transformation of the tetragonal zirconia into its monoclinic phase.

The high-resolution electron microscopy analysis confirms the formation of the solid solutions when samples were annealed at 560 °C. At this temperature two different type of crystalline regions were formed: One with nearly spherical morphology having an average diameter of 8 nm and a tungsten oxide concentration of 12.5 mol%. The other region type was larger with a non-spherical morphology, well-faceted faces and a tungsten oxide concentration of 9 mol%. When samples were annealed at 800 °C two type of zirconia crystallites were observed: Those with tetragonal and those monoclinic symmetry. Both types of crystallites were covered with patches of WO_3 nanocrystallites on their surface. The tetragonal structure was stable because not all tungsten atoms in the crystallite bulk segregated to its surface, while the monoclinic structure indicates that in the corresponding crystallites almost all tungsten in their bulk segregated to their surface. This tungsten segregation gave rise to the WO_3–ZrO_2 catalysts, contradicting the reported assumptions for these catalysts which claim that the corresponding crystallites are made of a tungsten oxide monolayer covering zirconia crystallite surface.

Acknowledgments

This work was financially supported by project IMP-D.00237. The authors thank Eng. German Vazquez and Dr. Juan Navarrete for technical assistance in XPS measurements.

References

[1] M. Hino, K. Arata, J. Chem. Soc. Chem. Commun. (1987) 1259.
[2] T. Yamaguchi, Appl. Catal. A 6 (1990) 1.
[3] G. Larsen, E. Lotero, R.D. Parra, L.M. Petkovic, H.S. Silva, S. Raghavan, Appl. Catal. A 130 (1995) 2131.
[4] E. Blomsma, J.A. Martens, P.A. Jacobs, J. Catal. 159 (1996) 323.
[5] M. Hino, K.J. Arata, Chem. Soc. Chem. Commun. (1980) 851.
[6] T. Yamaguchi, K. Tanabe, J. Phys. Chem. 90 (1986) 4794.
[7] K. Tanabe, M. Misono, Y. Ono, H. Hattori, bnnbn, in: Studies in Surface Science. "New Solid Acids and Bases: Their Catalytic Properties", Vol. 1, Elsevier, Amsterdam, 1989.
[8] A. Hofmann, J. Sauer, J. Phys. Chem. B (2004) 14652.
[9] K. Rajesh, P. Mukundan, K. Pillai, V.R. Nair, K. Warrier, Chem. Mater. 16 (2004) 2700.
[10] E. López, J. Hernández, M.A. Cortés, J. Navarrete, M.E. Llanos, A. Vázquez, H. Armendáriz, T. López, Appl. Catal. A 175 (1998) 43.
[11] J.G. Santiesteban, J.C. Vartuli, S. Han, D. Bastian, C.D. Chang, J. Catal. 168 (1997) 431.
[12] S. Xie, K. Chen, A.T. Bell, E. Iglesia, J. Phys. Chem. B 104 (2000) 10059.
[13] D. Barton, S.L. Soled, D. Meitzner, G.A. Fuentes, E. Iglesia, J. Catal. 181 (1999) 57.
[14] M.L. Pérez, J.A. Toledo, A. Montoya, R. Rosas, Catal. Lett. 97 (2004) 59.
[15] W.E. Alvarez, H. Liu, D.E. Resasco, Appl. Catal. A 162 (1997) 103.
[16] R.A. Boyse, E. Ko, J. Catal. 171 (1997) 191.
[17] M. Occhiuzzi, D. Cordischi, D. Gasoil, M. Valigi, P. Heydorn, Appl. Catal. A 269 (2004) 169.
[18] D.A. Ward, E.I. Ko, J. Catal. 150 (1994) 18.
[19] R.A. Boyse, E. Ko, Catal. Lett. 38 (1996) 225.
[20] M.A. Cortés, J.A. Toledo, H. Armendáriz, I. Hernández, X. Bokhimi, J. Solid State Chem. 164 (2002) 339.
[21] D. Barton, M. Shtein, R. Wilson, S. Soled, E. Iglesia, J. Phys. Chem. B 103 (1999) 630.
[22] J.A. Horsley, I.E. Wachs, J.M. Brown, Via, G.H. Hardcastle, J. Phys. Chem. B 91 (1987) 4014.
[23] D.S. Kim, M. Ostromecki, I. E Wachs, S.D. Kohler, J.G. Ekerdt. Catal. Lett. 33 (1995) 209.
[24] S. Utsunomiya, R.C. Ewing, Environ. Sci. Technol. 37 (2003) 786.
[25] M. Jouanne, J.F. Morhange, M. Kanehise, E. Haro-Poniatowski, G.A. Fuentes, E. Torres, E. Hernández-Tellez, Phys. Rev. B 64 (2001) 155404.
[26] S. Loridant, C. Feche, N. Essayem, F. Figueras, J. Phys. Chem. B 109 (2005) 5631.

[27] D. Di Gregorio, V. Keller, J.Catal. 225 (2004) 45.
[28] P. Jian, G.Z. Lu, Y.Y. Li, Chem. Lett. 33 (2004) 1064.
[29] J.A. Badenes, M. Llusar, J. Calbo, Br. Ceram. Trans. 101 (2002) 154.
[30] T. Masui, K. Nakano, T. Ozaki, G. Adachi, Z. Kang, L. Eyring, Chem. Mater. 13 (2001) 1834.
[31] X. Bokhimi, A. Morales, A. García-Ruiz, T.D. Xiao, H. Chen, P.R. Strutt, J. Solid State Chem. 142 (1999) 409.
[32] J.A. Dean, Lange's Handbook of Chemistry., 14th ed., Mcgraw-Hill, New York, 1992, p. 4.17.
[33] E. Torres, G. Rosas, J.A. Ascencio, E. Haro, R. Perez, Appl. Phys. A 79 (2004) 401.
[34] N. Naito, N. Katada, M. Niwa, J. Phys. Chem. B 103 (1999) 7206.
[35] P.L. Hansen, J.B. Wagner, S. Helveg, J.R. Rostrup-Nielsen, B.S. Clausen, H. Topsøe, Science 295 (2002) 2053.
[36] J.R. Sohn, M.Y. Park, Langmuir 14 (1998) 6140.
[37] M. Scheithauer, T.K. Cheung, R.E. Jentoft, R.K. Grasselli, B.C. Gates, Knözinger, J. Catal. 180 (1998) 1.
[38] C.D. Baertsch, S.L. Soled, E. Iglesia, J. Phys. Chem. B 105 (2001) 1320.
[39] S. Kuba, M. Che, R.K. Grasselli, J. Phys. Chem. B 107 (2003) 3459.